Jet-jet interaction in multiple injections: A large-eddy simulation study

Hadadpour, Ahmad; Jangi, Mehdi; Bai, Xue-Song

Published in:
Fuel

DOI:
10.1016/j.fuel.2018.07.010

2018

Please cite this article as: Hadadpour, A., Jangi, M. and Bai, X.S., Jet-jet interaction in multiple injections: A large-eddy simulation study. Fuel (2018), 234, pp.286-295. https://doi.org/10.1016/j.fuel.2018.07.010.

Jet-jet interaction in multiple injections: a large-eddy simulation study

Ahmad Hadadpour[a], Mehdi Jangi[b,a,*], Xue Song Bai[a]

[a] *Division of Fluid Mechanics, Department of Energy Science, Lund University, P.O. Box 118, S 221 00 Lund, Sweden*
[b] *Department of Mechanical Engineering, School of Engineering, University of Birmingham, Edgbaston, Birmingham, B15 2TT*

Abstract

This paper reports on studies of multiple-injection strategies of gaseous fuel in a model combustion chamber and the role of jet-jet interactions on the mixing processes in the chamber using large-eddy simulation (LES). A high-pressure non-reacting gas flow injected through a jet with a nozzle diameter of 1.35 mm into a quiescent inert air environment is considered. First, we validate the method and our computational setup by comparing the simulation results of a single injection case with available experimental data. It is shown that the transient ensemble-averaged LES results agree well with the experimental measurements. Second, we simulate and compare fourteen injection strategies in order to understand the effect of the main and the post-injections duration, the dwell time and the mass flow rate of post-injection on the mixing, jet penetration, and near-nozzle mixture. The contribution of each injection in the local mixture composition is quantified by solving transport equations for the mixture fraction of each injection.

The results show that the turbulence generated in the main injection is enhanced when the post-injection flow into the main injection flow. The increase of the local turbulence intensity is in favor of increasing the scalar dissipation rate and enhancing the mixing rate. However, the penetration of the post-injection flow into the main injection flow and the level of the gas flow from the interaction of two injections depend on the dwell time and the momentum of the post-injection.

The results also show that the post-injection modifies the near-nozzle mixture. The comparison of cases with different mass flow rates in the post-injection indicates that the momentum of the post-injection can be optimized either to push away the near-nozzle remaining gas from the main injection and reduce the near-nozzle residue by more than 25% or enrich this fuel-lean region and increase the near-nozzle gasses by more than 43%. These results are very interesting for optimization of the post-injection to reduce engine-out emissions.

Keywords: Multiple-injection, Post-injection, Diesel engine, Mixing, LES, Near-nozzle residue

*Corresponding author.
E-mail address: m.jangi@bham.ac.uk

Graphical abstract

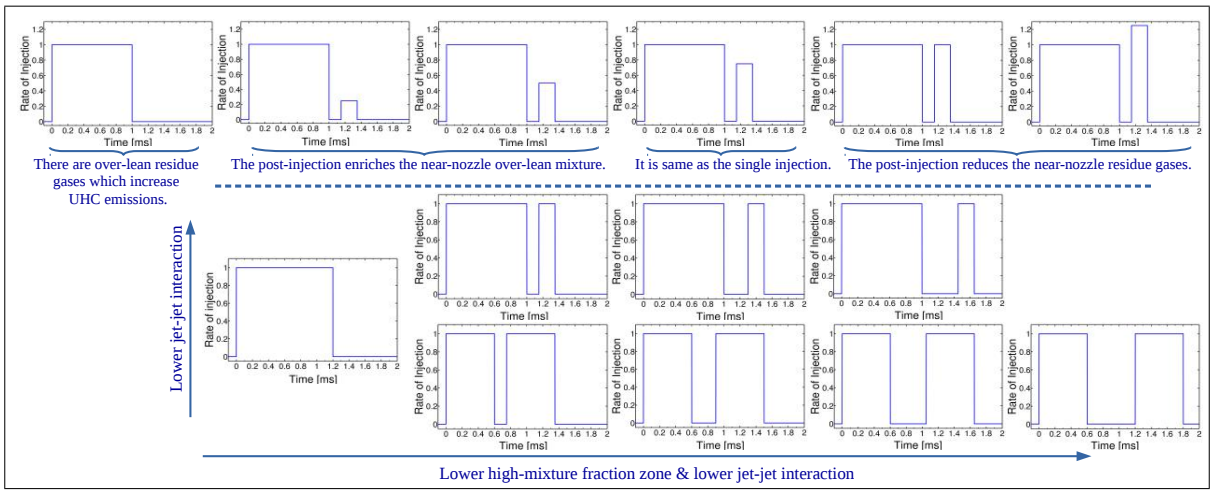

Highlights

- A high-momentum short post-injection reduces the near-nozzle residue gases.
- A low-momentum short post-injection enriches the near-nozzle over-lean mixture.
- The longer the dwell time, the lower the peak mass of the fuel-rich mixture.
- The cases with shorter dwell time and longer post-injection have more significant jet-jet interaction.

1. Introduction

Emissions in diesel engines can be reduced by either in-cylinder treatments or after-treatments. One of the common in-cylinder treatments is multiple-injection, which refers to adding a small post-injection of fuel after the end of the main injection [1] or to splitting the main injection into multiple smaller injections [2]. Previous studies showed various effects of the multiple-injection on the engine performance and emissions behavior [3]. For instance, Moiz et al. [4] studied the double injection of n-dodecane in a constant volume vessel and reported that the multiple-injection method can be beneficial for combustion efficiency. As another example, O'Connor et al. [5] investigated the effect of post-injection on unburned hydrocarbons (UHC) emissions and reported a 34% reduction of UHC in comparison to a single-injection case at the same load. Moreover, Hessel et al. [6] studied soot formation/oxidation for an engine-like condition and concluded that a short post-injection leads to a lower engine-out soot.

Despite many reports on the effects of the multiple-injection strategies, the underlying physics involved in such flow are still not fully understood. In an extensive review, O'Conor et al. [3] pointed out a number of remaining research questions, and summarised three main possible effects of multiple-injection: enhanced mixing [7–10]; increased combustion tempreture [11–14], and the injection duration effects [1, 15–17].

According to detailed soot formation and oxidation modeling [18], soot formation is most seen within a range of temperature and equivalent ratio (ϕ). For example for n-heptane combustion at a pressure of 60 bar, the equivalence ratio should be above 2. To gain a deeper understanding of the underlying physics of multiple-injection, we performed a systematic LES study of a non-reacting multiple-injection gas jet. The case is chosen based on a study by Hu. et al [19], in which a transient single-pulse gas injection into ambient air at atmospheric pressure was studied in order to investigate the gas-phase mixing in decelerating jets for practical engine application. We first simulated the same transient single injection case to compare our results with their work and validated our simulation. Then, we used this validated setup to study different multiple-injection strategies.

In this work, we model only the gas phase in order to avoid the uncertainties in the modeling of primary and secondary atomization processes of the spray. Instead, we made a great effort to properly model the mixing processes in the gas-phase by performing detailed LES calculations. The same approach has been used in literature, for instance, see Refs [19, 20]. While the size of nozzle diameter, hence the size of the potential core of the injected liquid fuel, in modern engines is of the order of 0.1 mm, in this approach the chosen size of the nozzle is of the order of 1 mm. For instance, in Ref [20] the chosen diameter for the measurement is 1 mm and in Ref [19] the chosen diameter for LES is 1.35 mm. The rationale behind the selection of the parameters for such studies is to choose the right injector diameter and the momentum of the jet that mimic the conditions of spray flows in engines [21, 22]. Our previous work on diesel spray [23] also confirmed that the diameter of the gas-phase spray is approximately 10 times larger than the diameter of the liquid injector.

In this study, with the goal of providing insight into gas-phase mixing and interaction of two injections, we strive to answer the following questions: (1) To what degree does the post-injection penetrate into and interact with the main injection? (2) By which mechanism can the post-injection enhance the mixing of injected gas with ambient air? (3) Does the penetration of the main injection change by having post-injection? (4) Is the turbulence in the main injection enhanced by the post-injection? (5) How is the mixture in the near-nozzle region affected by the post-injection strategy? (6) What is the effect of different parameters, such as dwell time, post-injection duration and mass flow rate of the post-injection on the answer to these questions?

2. Case specification and numerical method

As a baseline case for the validation of the numerical method and the solver, we have chosen the study of Hu, et al. [19]. They simulated a high-pressure single injection gas jet through a 1.35 mm diameter nozzle into the ambient air at atmospheric pressure and compared the results with an available experiment [24, 25]. In these experiments, the gas was injected for 4 ms and the mean axial velocity was measured along the centerline during and after the injection. The experiments reported an ensemble-average of velocity that was calculated from an ensemble of 100-500 measurements at each condition. The nearest data point that was measured in the experiments was at 2.9 mm from the nozzle. In the simulations, the inflowing mass flow rate was selected to match up the mean velocity at 2.9 mm. This gives a velocity of 90 m/s at the nozzle exit and the mass flow rate of 125 mg/s, approximately.

The computational domain is a cylinder with a diameter of 50D and a length of 100D, where D=1.35 mm is the nozzle diameter (Fig. 1a). The nozzle is placed in the center of the domain base. A cylindrical O-grid mesh is used, which consists of 2.3 million cells (Fig. 1b). The grids are refined toward the nozzle exit and across the jet axis such that 80% of computational cells are located within the refinement cylinder 10D×25D.

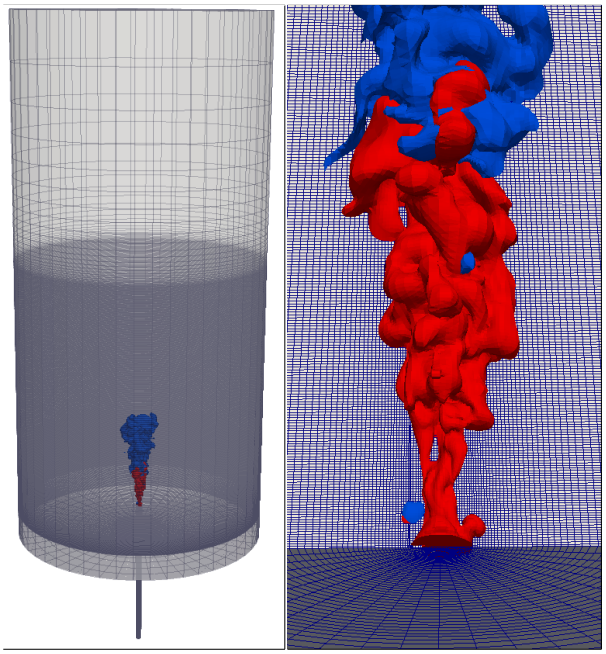

Figure 1: (a) Computational domain. Domain diameter=50D and length=100D, where D=1.35 mm is the nozzle diameter. The length of auxiliary inlet pipe is 30D; (b) The grid near the nozzle. The red and blue surfaces are iso-countours of mixture fraction in the first injection and second injections, respectively.

It is known that the modeling of turbulent inlet velocity boundary conditions in LES requires special care. For example, imposing a turbulent inlet velocity boundary condition with only white noise fluctuations is inappropriate as such noises will quickly dissipate within a few nozzle diameters and the flow will not develop into large-scale fluctuations. In this work, to achieve an appropriate inlet boundary condition for the injector, in addition to the main domain, a long auxilliary inflow pipe is simulated. A radial velocity component is added to the inlet boundary condition of the pipe to boost the instabilities. This radial velocity creates a large vortex at the early stage of the auxiliary pipe. This vortex brakes down to eddies and boosts the turbulence. The length of the pipe is chosen to be long enough (30D) to achieve a symmetric mean flow profile at the outlet of the pipe. Simulation results at the outlet of the pipe, which are temporally evolving, are used as the inlet boundary condition for the main flow domain calculations. To achieve various LES realizations of a case (Cases in Table 1), the radial component of velocity at the inlet of the auxiliary pipe is changed. As a result, while the profile of the mean velocity at the outlet of the pipe does not change, the instantaneous velocity profile is different for various realizations. For the walls and outlet velocity boundaries, the no-slip and zero-gradient conditions are imposed respectively.

OpenFOAM is used for numerical solution of spatially filtered Navier-Stokes (N-S) equations for incompressible flow. Both temporal and spatial terms are discretized using implicit second-order schemes. Dynamic k-equation is used as the sub-grid scale (SGS) model in the LES. In addition to the N-S equations and the SGS k-equation, two mixture fraction transport equations are solved to trace each injection.

$$\frac{\partial \overline{\rho}\tilde{Z}_i}{\partial t} + \frac{\partial \overline{\rho}\tilde{u}_j\tilde{Z}_i}{\partial x_j} - \frac{\partial}{\partial x_j}\left[\overline{\rho D}\frac{\partial \tilde{Z}_i}{\partial x_j} + \Phi^{sgs}_{Z_i}\right] = 0 \tag{1}$$

where Z_i is the fraction mixture of the i-th injection, u_j is velocity component along x_j direction, ρ is density and $\Phi_{Z_i}^{sgs}$ is the subgrid mass flux. These two extra equations enable us to study the interaction between the main and post-injection, as well as the mixing of the injected gas with the ambient air. Hereafter, we refer the mixture fraction of the first and second injections to as Z_1 and Z_2, respectively. The total mixture fraction of the injected gas, Z_t, is the sum of the two mixture fractions $Z_t = Z_1 + Z_2$. The initial condition of Z_1 and Z_2 in the domain is set to 0. The boundary conditions at the nozzle exit for Z_1, and Z_2 during the first injection is set to 1 and 0, respectively, whereas they are set to 0 and 1, during the second injection. Both temporal and spatial terms of these mixture fraction transport equation are discretized using implicit second-order schemes.

3. Validation of the simulation

The validation of the simulation is done in two steps. Firstly, to check the grid independence, a steady jet flow (Case a) is simulated and the result is compared with available experiments. Secondly, the same jet but with short single injection (Case b) is simulated and the accuracy of the simulation of the transient jet is investigated. Once the accuracy of the numerical method and the computational setup are confirmed, the same settings are used to investigate multiple-injection cases (cases 1-14).

3.1. Steady jet simulation for grid independence study

To examine the grid independence, a steady jet flow is simulated and the results are compared to the available experiment. To achieve the quasi-steady state in the simulation, the steady jet flow is simulated for 15 ms (Case a in Table 1). The first 3 ms is considered as transient jet flow and after that time-averaged axial velocity along the centerline is calculated. The jet velocity at the nozzle exit in this simulation is set to 90 m/s. According to the literature [26], the time-averaged axial velocity along the axis of a steady jet is a linear function of the inverse of axial position:

$$\frac{U_0(x)}{U_j} = \frac{B}{(x - x_0)/D} \tag{2}$$

where x is the axial distance from the jet outlet, x_0 is a virtual origin, $U_0(x)$ is the mean axial velocity at the center of the jet at x, U_j is velocity at $x = 0$, D is the nozzle diameter and B is velocity-decay constant which is an empirical constant and independent of Reynolds number. It must be mentioned that this equation is not valid in the initial development region of the jet.

We used different grids and calculated the value of velocity-decay constant. The topologies of the grids are the same, but the cell sizes are changed. Five different grids are employed, with the normalized averaged size of cells (normalized with the diameter D) at the nozzle exit (Δh^*) ranging from 0.04 to 0.08. The baseline grid consists of 2.3 million cells and $\Delta h^* = 0.046$. In Fig. 2 the value of B from different grids are compared to the experiment data of Hussein et al. [27]. The measured B in the experiment is 5.8 and with the baseline grid, the difference between the calculated B in LES and experiment is 3.6%.

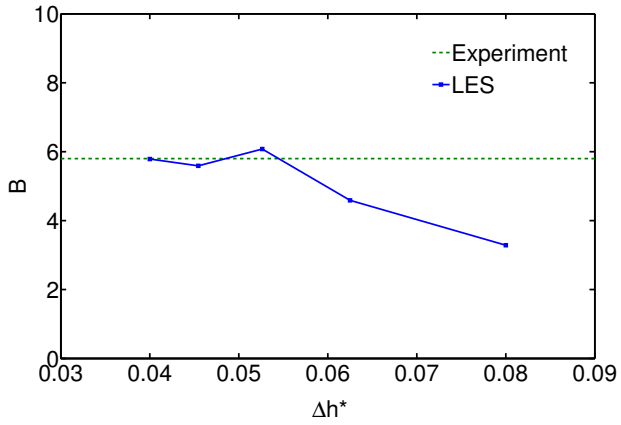

Figure 2: Calculated velocity-decay constant. $\Delta h^* = \Delta h/D$ where Δh is the size of the cell in the injector outlet and D is the diameter of the injector. By reducing the size of cells, the value of B in LES converges to the measured value in the expriment in Ref. [27]

In addition to axial profile the radial profile of the mean axial velocity is investigated. In a turbulent round jet, the radial profiles of the mean axial velocity in different axial positions beyond the developing region are self-similar [26, 27]. In other words, profiles of $U(x,r)/U_0(x)$ as a function of $r/(r_{1/2}(x))$ in different axial positions collapse into a single profile. $U(x,r)$ and $U_0(x)$ are the mean axial velocity at (x,r) and $(x,0)$ respectively, r is the radial distance to the axis, and $r_{1/2}(x)$ is the jet's half-width radius, defined as:

$$U(x, r_{1/2}) = \frac{1}{2}U_0(x) \tag{3}$$

In Fig. 3 the radial profiles of the steady jet flow at different axial positions are compared to the results from Ref. [26]. As can be seen in this figure, all radial profiles are collapsed into a single curve, which indicates a self-similar velocity distribution across the jet axis.

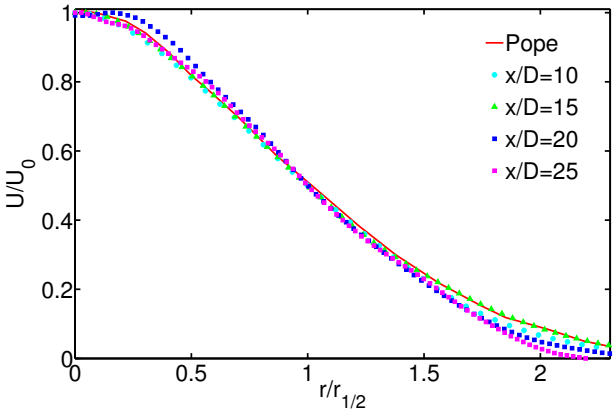

Figure 3: Self-similarity of radial profiles of the mean axial velocity in the steady jet at different downstream locations. Predicted $r_{1/2}(x)$ at $x/D = 10,\ 15,\ 20$ *and* 25 are 1.61, 2.18, 3.09 and 3.74 *mm*, respectively. The radial profiles are compared to the curve from Ref. [26]

The jet spreads linearly and the spreading rate is defined as [26]

$$S \equiv \frac{dr_{1/2}(x)}{dx} \tag{4}$$

The calculated spreading rate in the LES is 0.1025 and matches well with the measured values. The measured values of the spreading rate using two different measurement techniques are 0.102 and 0.094 [27]. The predicted cone angle of the jet is 11.74°. This angle is calculated by considering axial velocity equal to $1m/s$ as the outer limit of the jet.

3.2. Validation of transient jet simulation

The transient jet flow case studied here is taken from the expriment [24] and simulations [19]. The jet has the same configuration as the steady flow discussed in Section 3.1, but a shorter injection duration (Case b in Table 1). The inlet gas has a top-hat time profile, with an inlet velocity of 90 m/s for $0 < t < 4ms$. The baseline grid is used in the steady jet case used in the present transient jet simulation. Each transient case can be divided into three phases, ramp up, quasi-steady, and ramp down periods. To be able to study multiple-injection, the simulation must be able to replicate these three phases. Fig. 4 shows the ensemble-averaged centerline velocity at various downstream locations during and after the injection. Solid red lines show the present prediction, the blue dashed line and the green dashed-dot line show the measurement in the experiments [24] and the results of Hu et al. [19], respectively. In the experiments, the ensemble-averaged velocity over 100-500 injection events is reported. In current work, to calculate the ensemble-averaged values, each calculation was repeated 20 times with a different instance of the inlet velocity boundary conditions generated from the inflow pipe simulation, as discussed early. Fig. 5 shows the distribution of the mass fraction of the injected gas at $t = 1.2ms$. While the large-scale eddies can be observed in the single realization instantaneous field (Fig. 5a), the ensemble-average over 20 realizations (Fig. 5b) shows a symmetric distribution of variables and a smoother field.

As can be seen (Fig. 4), the current results agree well with the experimental results. The velocity magnitude in the quasi-steady phase has been well predicted, with some minor under-predictions at a few locations. These deviations are most likely due to the inconsistency in the injector boundary condition. It is noted that the injector used in the experiment had a complex geometry, whereas we used a simplified inflow pipe in these simulations. Nonetheless, the transient flow velocity in the ramp up ($0 < t < 1.5$), quasi-steady ($1.5 < t < 4$) and ramp down ($4 < t < 6$) stages are captured reasonably well. This can be confirmed once we compare our results with the simulation results from Hu et al. [19] for the same conditions.

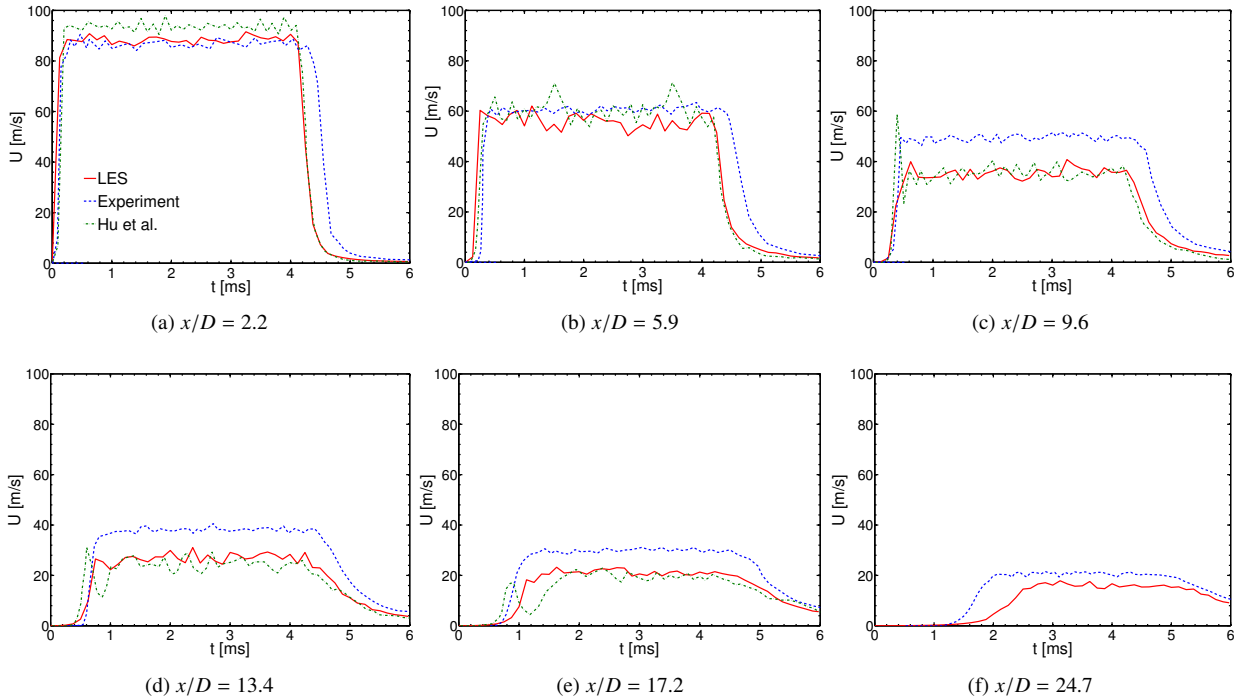

(a) $x/D = 2.2$ (b) $x/D = 5.9$ (c) $x/D = 9.6$

(d) $x/D = 13.4$ (e) $x/D = 17.2$ (f) $x/D = 24.7$

Figure 4: Ensemble-averaged centerline axial velocity at various downstream locations; present prediction, the measurement in the experiments [24] and the results of Hu et al. [19].

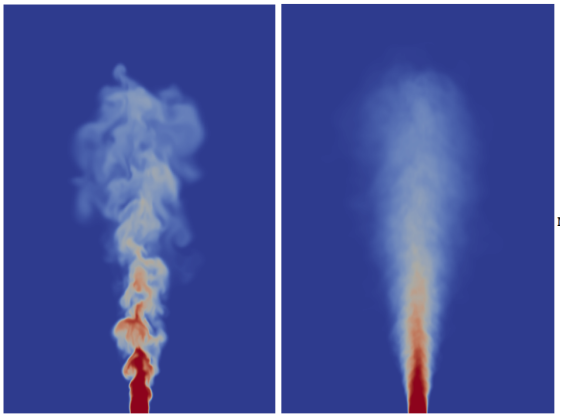

(a) (b)

Figure 5: Mass fraction of the injected gas at t=1.2 ms. (a) LES instantaneous field; (b) Ensemble-averaged field over 20 LES realizations;

3.3. Resolved fraction of the turbulence

The resolved scale turbulent kinetic energy, k_{res}, is defined as:

$$k_{res}(x, y, z, t) = \frac{1}{2}((u')^2 + (v')^2 + (w')^2) \tag{5}$$

where $u' = u - \langle u \rangle$ is the fluctuation of axial velocity, and v' and w' are the corresponding ones of the other two velocity components. The turbulence kinetic energy can be calculated from the ensemble-average of resolved scale turbulent kinetic energy, $\langle k_{res} \rangle$, and the subgrid-scale turbulent kinetic energy, $\langle k_{sgs} \rangle$.

$$\langle k(x, y, z, t) \rangle = \langle k_{res}(x, y, z, t) \rangle + \langle k_{sgs}(x, y, z, t) \rangle \tag{6}$$

where $\langle \rangle$ denotes ensemble average with the 20 LES runs. Fig. 6a and 6b show the instantaneous distribution of k_{res} and k_{sgs} respectively, in a single realization at $t = 1.2ms$. A logarithmic scale is used in this figure. Comparing these two fields shows what fraction of turbulence is resolved in the simulation. To compare it quantitatively, the ensembled average of these fields with 20 LES realizations are calculated and the fraction of resolved turbulence kinetic energy (i.e. $\langle k_{res} \rangle / (\langle k_{res} \rangle + \langle k_{sgs} \rangle)$) is shown in Fig. 7. The curves show the calculated values at various downstream locations which are shown by white lines in 6. As can be seen, at least, 72% of turbulence kinetic energy is resolved. On average, more than 80% of turbulence kinetic energy is resolved.

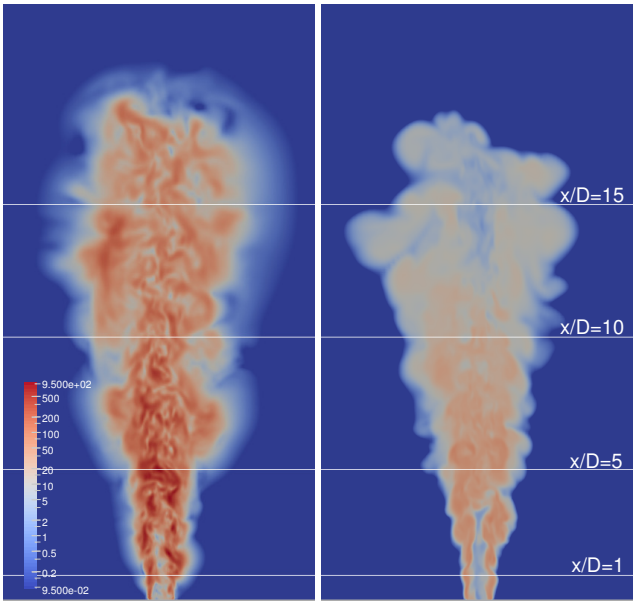

(a) (b)

Figure 6: The instantaneous distribution of turbulent kinetic energy at $t = 1.2ms$. (a) resolved scale kinetic energy, k_{res}; (b) modeled sub-scale kinetic energy, k_{sgs}; A logarithmic scale is used.

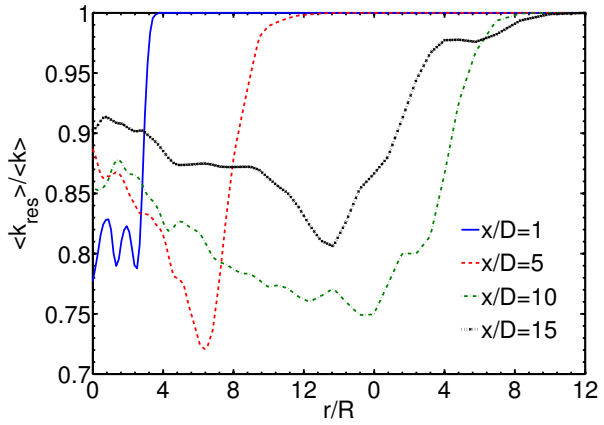

Figure 7: The fraction of resolved turbulence kinetic energy, $\frac{\langle k_{res}\rangle}{\langle k_{res}\rangle+\langle k_{sgs}\rangle}$. r is the radial distance and R is the radius of the nozzle. The downstream location of the plots are shown by white lines in Fig. 6

4. Results and discussion

4.1. Specification of multiple-injection strategies

To define realistic injection strategies, real engine experiments in Refs. [28, 29] are considered. In Ref. [28], a single injection is split into a main 970 μs injection plus a short 200 μs post-injection. In Ref. [28], the actual start of the main and post-injections are -5 and 3 ATDC (after top-dead-center) respectively, and the engine speed is 1200 rpm. To mimic the injection strategy, we set the main injection, dwell and post-injection durations to 1, 0.15 and 0.2

Table 1: Specification of injection strategies (Cases a and b are used for the grid study and validation of the simulation, using the availabe measurements. Cases 6 and 13 are identical.

	First injection duration (ms)	Interval duration (ms)	Second injection duration (ms)	$\dot{m}_{inj2}/\dot{m}_{inj1}$
Case a	∞	-	-	-
Case b	4	-	-	-
Case 1	1.2	-	-	-
Case 2	0.6	0.15	0.6	1
Case 3	0.6	0.3	0.6	1
Case 4	0.6	0.45	0.6	1
Case 5	0.6	0.6	0.6	1
Case 6	1	0.15	0.2	1
Case 7	1	0.3	0.2	1
Case 8	1	0.45	0.2	1
Case 9	1	-	-	-
Case 10	1	0.15	0.2	0.25
Case 11	1	0.15	0.2	0.5
Case 12	1	0.15	0.2	0.75
Case 13	1	0.15	0.2	1
Case 14	1	0.15	0.2	1.25

ms, respectively (Case 6 in Table 1). We investigate the effects of injection timing by studying further six different strategies and a single injection strategy (Cases 1-8). In these cases, the total amount of injected mass is the same and the total time in which the injector is open is 1.2 ms, the same for all cases.

In cases 2, 3, 4 and 5, shown in Table 1, the injection time is split into two equal injections. The dwell times in these cases are 0.15 ms, 0.3 ms, 0.45 ms and 0.6 ms, respectively. In cases 6, 7 and 8 the injection is split into a long main injection and a short post-injection, 1 and 0.2 ms, respectively. The dwell times in these cases are 0.15, 0.3 and 0.45 ms. In cases 2-8, the injection rate of the first and the second injection are the same. Cases 2 and 6 are the same as those presented in our previous study here the effect of splitting timing was observed [30]. In addition to the presented cases here, cases 9-14 are simulated (The results will be presented in section 4.4) to study the effect of post-injection on the near-nozzle mixture. These post-injection cases have the same timing as case 6, but the mass flow rates of the post-injection are different.

It should be noted that for each of these cases, 20 realizations are simulated and the ensemble-averaged values are calculated for analysis. This means that the analysis and results presented here are based on more than 200 LES calculations.

4.2. The jet-jet interaction

An important process in multiple-injection strategies is the interaction between two injections. When two injections interact, the turbulence intensity in the high-mixture-fraction zone of the first injection is increased and its mixing with ambient air is enhanced. Subsequently, the amount of mass of high mixture fraction from the first injection reduces. This effect is sensitive to the dwell time and the duration of the second injection. To show this effect and its sensitivity to the dwell timing, we examine the distribution of the probability density function (PDF) of Z_1 (see Fig.8) for various dwell timings. In these cases, the duration of the main and post injections are the same while the dwell times are varying between 0.15-0.6 ms (Table 1). Shown in Fig.8 are the results at t=1.8 ms after the start of injection (ASI) when both injections have already finished. As can be seen in this figure the probability of the fuel rich mixture, e.g., $Z_1 > 0.08$, has been significantly affected by the dwell timing. For example, in case 2 with the shortest dwell time of 0.15 ms, the PDF of Z_1 has a much smaller extension to the high mixture fraction values.

The Z_1 distribution in case 3 is also slightly modified by the second injection whereas for cases 4 and 5 in which the dwell time is greater than 0.3 ms the PDF of Z_1 is less sensitive to the post-injection. This implies that the level of interaction of the two injections is highly sensitive to the dwell time.

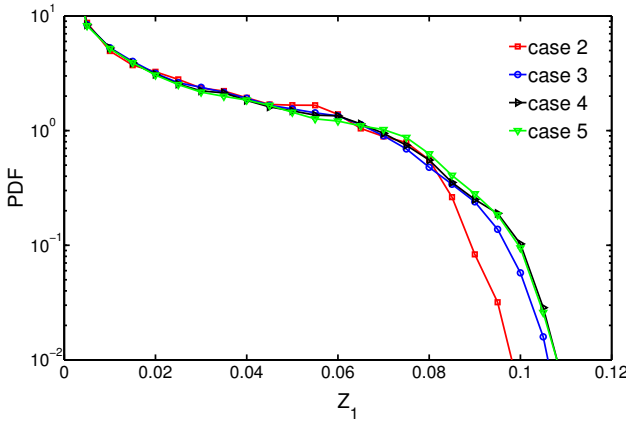

Figure 8: The probability density function of mixture fraction of injected gas from the first injection, Z_1, at t=1.8 ms ASI. Case 2, which has the shortest dwell time among the cases, has the lowest PDF at high Z_1.

Fig.9 shows the turbulence kinetic energy distribution ($\langle k_{res} \rangle + \langle k_{sgs} \rangle$) for cases 2-5 after 0.45 ms from the end of the second injection, e.g., at t=1.8 ms, 2 ms, 2.1 ms, and 2.3 ms ASI for cases 2, 3, 4, and 5, respectively. The results imply that the penetration of the second injection into the first injection can potentially increase the local turbulence intensity, hence increases the mixing process. As can be seen here, although the second injection penetration for all cases is almost the same, the overlap between the first and second injections in each case is different. Especially, when comparing the results in Fig.9a with that of Fig.9d, one can readily observe that high turbulence intensity of the second injection has largely overlapped with the first injection in case 2, whereas it barely touches the first injection in case 5. Obviously, when the post-injection efficiently penetrates into the first injection, similar to that in Fig.9a, it increases the local turbulence intensity and enhances the mixing. On the other hand, in Fig.9d, although the post-injection has high turbulence intensity, however, due to a very long dwell timing it does not interact with the first injection.

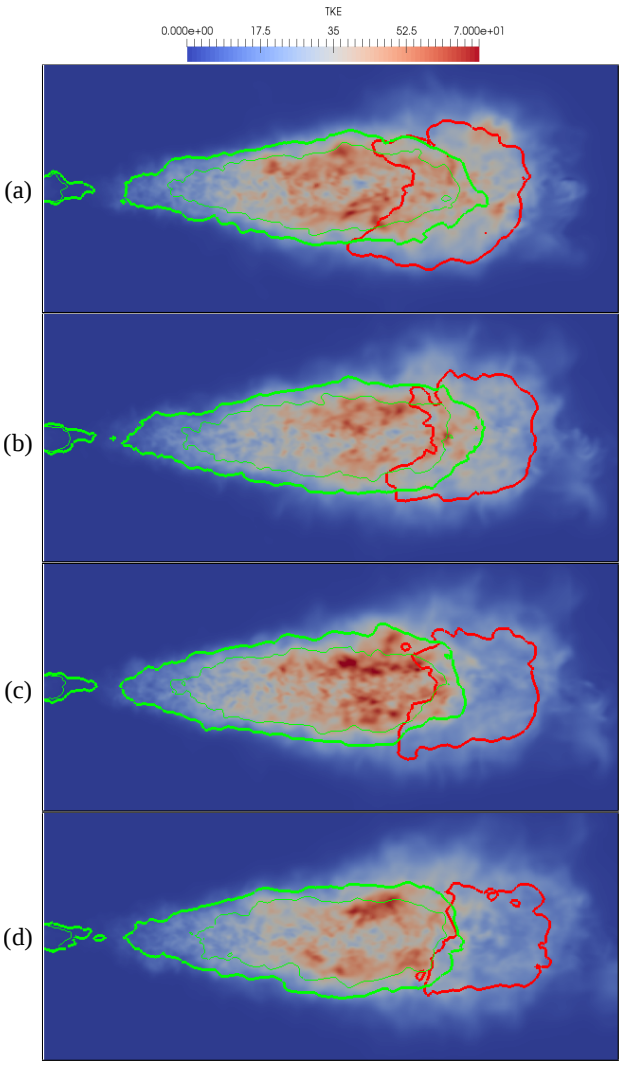

Figure 9: Ensemble-averaged turbulence kinetic energy; (a) case 2 at t=1.8 ms; (b) case 3 at t=2 ms; (c) case 4 at t=2.1 ms; (d) case 5 at t=2.3 ms. Each frame shows $35cm \times 15cm$. The lines are iso-contours of mixture fraction of injected gas. The thick red line is $Z_1 = 0.05$, the thin red line is $Z_1 = 0.1$, the thick green line is $Z_2 = 0.05$ and the thin green line is $Z_2 = 0.1$. (The region with $Z_2 > 0.1$ is too small at these instance, therefore, the thin red line is hardly visible. The thin red line is visible, for example, in Fig. 11)

We further examine this idea by considering the scalar dissipation rate at different dwell timing. Generally speaking, the higher turbulence intensity increases the local scalar dissipation rate, hence, enhances the mixing quality. The scalar dissipation rate can be calculated in terms of fraction variable as below [31, 32]:

$$\chi = 2(D_Z + D_t)(\nabla Z)^2 \tag{7}$$

where D_Z is the molecular diffusivity of the mixture fraction, D_t is sub-grid eddy diffusivity and ∇Z is the gradient of the mixture fraction on the resolved scale. Fig. 10 shows the ensemble average of $(\nabla Z_1)^2$. As seen here, with a shorter dwell timing of case 2, the ensemble average of $(\nabla Z_1)^2$ is higher as a result of the interaction of the two injections. For instance, comparison of Figs. 10a and 10d shows that the scalar dissipation rate in case 2 is significantly larger than that in case 5.

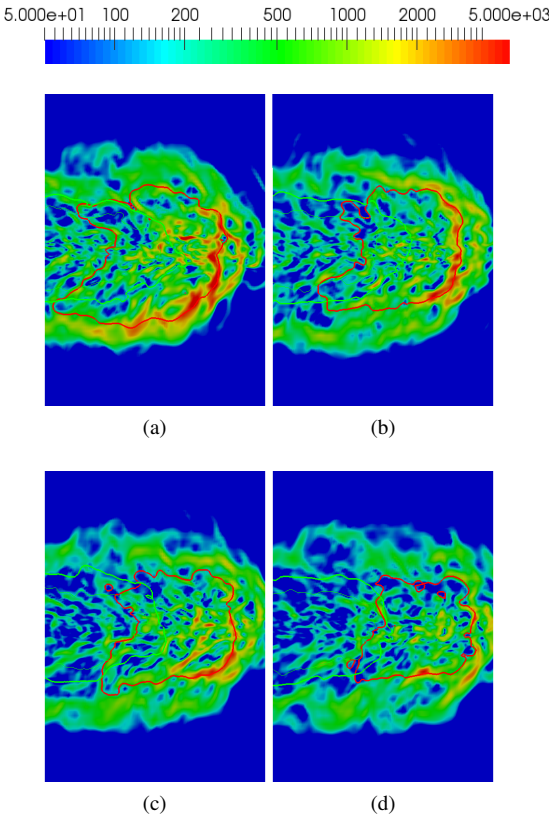

Figure 10: Ensemble averege of $(\nabla Z_1)^2$; (a) case 2 at t=1.8 ms; (b) case 3 at t=2 ms; (c) case 4 at t=2.1 ms; (d) case 5 at t=2.3 ms; Each frame showsa domain of $14cm \times 20cm$. Lines are iso-contour of Z_1 and Z_2, for more detail see the caption of Fig. 9.

In addition to the dwell timing, another important factor influencing the level of interaction of two injections is the momentum of the post-injection. If the post-injection does not have enough momentum it cannot penetrate enough into the main injection and enhance its local turbulence mixing rate. Fig. 11 shows turbulence kinetic energy and iso-contours of Z_1 and Z_2 at 0.35 ms after the end of the second injection. In these cases, a single injection is split into a long main injection and a second short post-injections. Consistent with the previous discussion, here also the maximum penetration of the second injection into the first one occurs when the dwell time is the shortest, as can be seen in Fig. 11a. However, in all these three cases, the momentum of the post-injection is not large enough to significantly interact with the first injection and the second injection is only partially penetrating into the first one. In these cases, only in the tail of the first injection, the turbulence intensity is increased by the second injection. We will show further evidence in the next section about the effect of dwell time and duration of the second injection on the jet-jet interaction by studying the penetration of each of the injections.

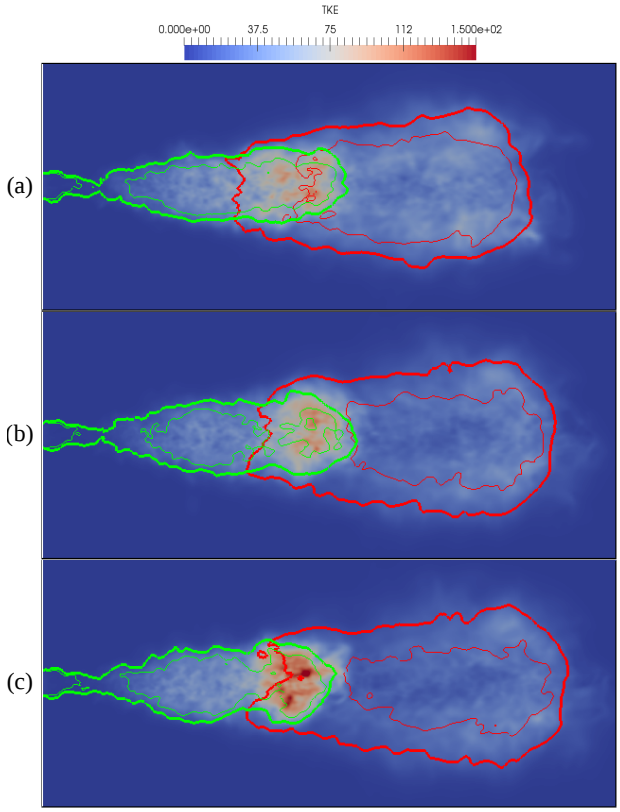

Figure 11: Ensemble-averaged turbulence kinetic energy. (a) case 6 at t=1.7 ms; (b) case 7 at t=1.9 ms; (c) case 8 at t=2 ms; Each frame shows $35cm \times 15cm$. Lines are iso-contours of Z_1 and Z_2, for more detail see the caption of Fig. 9.

4.3. Penetration

Figure 12a shows the overall penetration of the jet in all cases, which is calculated based on the farthest distance of the iso-countor $Z_t = 0.01$ from the nozzle exit. As mentioned before, in all cases the same amount of fuel is injected. The effects of the different splitting strategy and dwell time on the overall jet penetrations are almost negligible. Only in cases with too long dwell timing, for example, case 5, the penetration is slightly lower than that of the other cases. This is consistent with the literature [33].

Figure 12b shows the penetration of the first and the second injection in the domain for cases 2-5, in which the single injection is splitting into two equal injections (see Table 1). The penetration rate of the post-injection in all cases in Fig. 12b (the slope of the dashed lines) is slightly higher than that of the main injections (the slope of the solid lines). The reason is that the first injection is essentially discharging of the mass into a quiescent environment, whereas the second injection is influenced by history effects from the first injection. Interestingly, in Fig. 12b the second injections in all cases almost have the same penetration rate, especially at the beginning of the injection, regardless of their dwelling time. Another interesting observation is that the second injection tip always catches up the main injection's tip for all cases in Fig. 12b. In the cases with shorter dwell time, the catchup occurs faster in comparison to the cases with longer dwell time. This catch-up, however, is not the case for cases 6-8 (Fig. 12c) where there is always a gap between the tips of the first and the second infection. Considering that cases 6-8 consist of a long first injection and a short post-injection, these results indicate the importance of the kinetic energy available in the second injection. The results imply that with a small post-injection the kinetic energy of the second injection can quickly dissipate and the jet's tip cannot reach the main injection. Figures 12b-c support our discussion in the previous section and show that the penetration of the second injection into the first one, which can represent the interaction of two injections, is highly sensitive to the duration of dwell time (Fig. 12b) and the duration of the second injection (Fig. 12c).

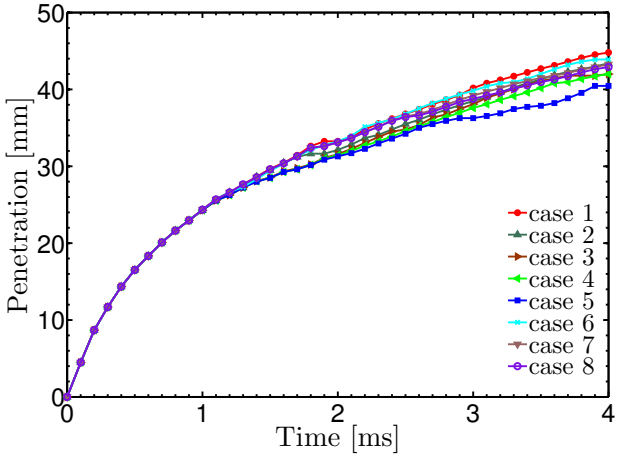

(a)

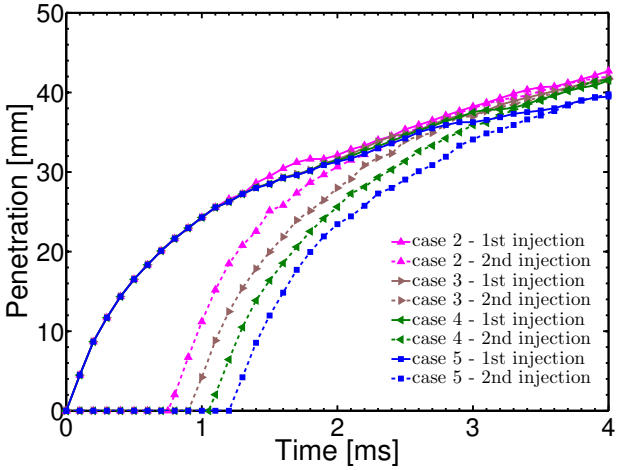

(b)

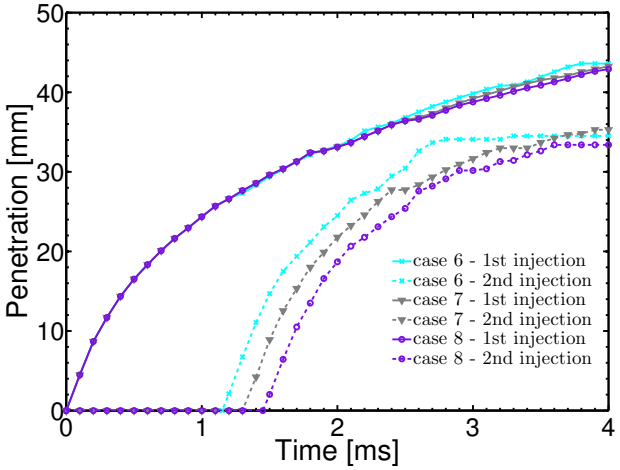

(c)

Figure 12: Penetraion of the main and the post-injections

4.4. Effects of post-injection strategies on the near-nozzle over-lean mixture

At the end of the main injection some of the injected gas remains near the nozzle (see Fig. 13a). This residue does not have enough momentum to penetrate into the domain. In diesel engines, it can increase the amount of UHC emissions. The second injection, potentially, can push the near-nozzle residue of the first injection and increase its momentum. However, the post-injection can leave the same residue near the nozzle, especially if it has the same mass flow rate and duration as the main injection. For example in Fig. 13b, the residue of the second injection can be seen near the nozzle and it totally resembles the residue of the main injection in Fig. 13a. It indicates that injection splitting does not necessarily lead to improvement of the near-nozzle gas mixture, which explains why in Chartier's experiments [28] the splitting a single injection into a main and a relatively long post-injection virtually had no effect on the UHC emissions. They observed that only some post-injection strategies can reduce engine-out UHC emissions.

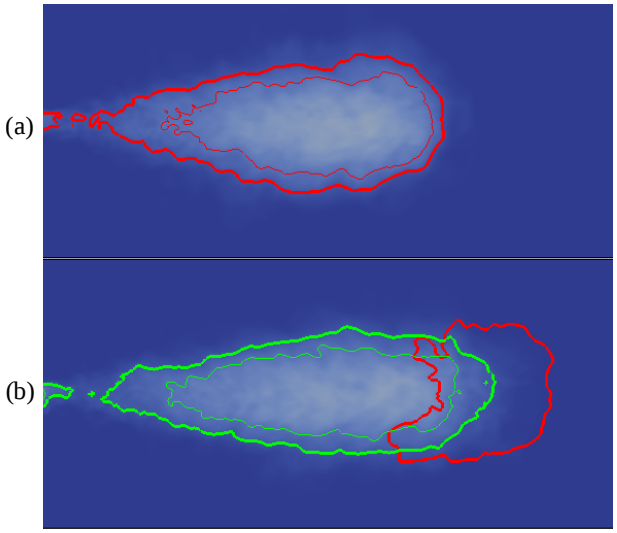

Figure 13: (a) Snapshot of ensemble-averaged Z_1 in case 5 at t= 1.1 ms; (b) Snapshot of ensemble-averaged Z_2 in case 3 at t= 2 ms.; Each frame shows a domain of $35cm \times 15cm$. Lines are iso-contour of Z_1 and Z_2, for more detail see the caption of Fig. 9.

To investigate the effect of post-injection on the near-nozzle mixture, we define and simulate six more cases (Cases 9-14 in Table 1). Injection timings in these cases are exactly the same as case 6. However, the mass flow rate of the second injection is not the same as the main injection. The ratios of the mass flow rate of the post-injection to the mass flow rate of the main injection in cases 10-14 are 0.25, 0.5, 0.75, 1 and 1.25 respectively. In case 9, there is no post-injection. Figure 14 shows the mass of the injected gas in the near-nozzle region at different times in these six cases. The near-nozzle region here is considered to be from the nozzle outlet to 10D downstream in the horizontal direction, where D is the diameter of the nozzle. The calculated mass of gas for each case is normalized to the mass of total injected gas for that case. The axial axis in this figure shows the time after the end of injection (EOI). The end of injection in cases 10-14 happens at the same time, but in case 9 which is a single injection, the end of injection happens earlier, at $t = 1ms$.

The plot of case 9 in Fig. 14 shows that around 5% of injected gas remains near the nozzle in a single injection strategy. Chartier et al. [28] showed that the near-nozzle residue is too lean to be ignited. They suggested that post-injection strategies can enrich this region and it was observed that only small injections can lead to this enhancement. Plots of cases 10-14 in Fig. 14 show that the amount of the gas is relatively high in the near-nozzle after the end of injection (see $0 < t < 0.5$ *ms EOI*). Obviously, the slope of these plots, especially in $0 < t < 1$ *ms EOI*, depends largely on the mass flow rate of the post-injection. In the cases with higher rate of injection, e.g. case 13 and 14, the injected gas has a high momentum and it leaves the near-nozzle region fast, hence the slope of this plot is higher and the near-nozzle ultimate residue in these cases is lower than that in the other cases (see $t > 1.5$ *ms EOI*). In cases with a small post-injection, e.g. cases 10 and 11, although the amount of injected gas in the post-injection is lower than that in the other cases, the ultimate residue is higher. In these cases, the small post-injection does not have enough

momentum to penetrate into the domain and most of it remains near the nozzle enriching the mixture in the region. It is consistent with the observation of Chartier et al. [28] that only small post-injection can enrich the near-nozzle fuel-lean region and reduce UHC emissions.

To conclude, the results show that a post-injection can be optimized either by increasing the momentum of the near-nozzle region that convects the accumulated gases near the nozzle further into the domain (e.g. cases 13 and 14), or by enriching the near-nozzle fuel-lean residue of the first injection (e.g. cases 10 and 11).

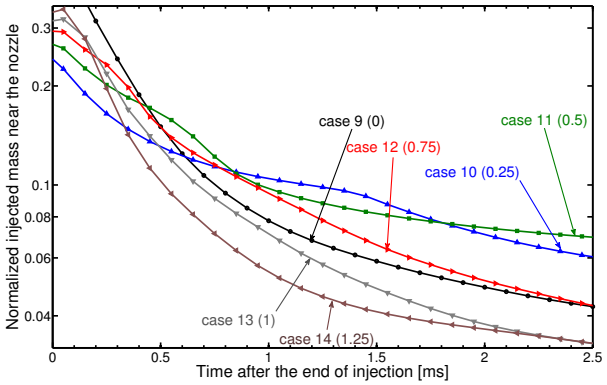

Figure 14: Normalized mass of the injected gas residing in the near-nozzle region. The near-nozzle region here is considered to be from the nozzle outlet to 10D downstream in the axial direction. In each case, the mass is normalized by the amount of total injected gas in the given case. The numbers in parentheses show $\dot{m}_{post-injection}/\dot{m}_{main\ injection}$.

4.5. The effect of dwell time on mixing

In this section, we examine the distribution of the overall mixture fraction from all injections, Z_t, to study the role of different injection strategies on the mixture formation process. Shown in Fig. 15 is the time history of the total mass of the region with a mixture fraction of $Z_t \geq 0.1$. It is known that in hydrocarbons combustion in engine applications, soot is primarily formed in the mixture with an equivalence ratio above 2. Considering the fact that most of the hydrocarbon fuels have a stoichiometric mixture fraction of around 0.05, the region with $Z_t \geq 0.1$ represents mixtures with an equivalence ratio greater than 2. In Fig. 15, case 1 is the single-injection case, and other cases are those from multiple-injection, while cases 2-5 have different dwell timing (see Table 1). As can be seen, in all multiple-injection cases, upon the start of the first injection the mass of the region with $Z_t \geq 0.1$ is increasing. After the end of the first injection at 0.6 ms, the mass of the region with $Z_t \geq 0.1$ keeps increasing for a short period of time after the end of the first injection. This is due to the mixing of the injected gas with the ambient air, which will continue even after the end of injection. While injection increases the mass of the region with $Z_t \geq 0.1$, the mixing and air entrainment act in opposite direction to diminish the fuel rich regions. Once the effects of entrainment and mixing become stronger than the effect of injection, the slope of curves become negative. This occurs at about 1 ms from the start of injection for cases 4 and 5. However, for cases 2 and 3 the dwell time is so short and the second injection is so close to the first injection, there is no time for the slope of the curve to become negative before the end of the second injection.

Nevertheless, the effects of injection dwell time, between the end of the first injection and the start of the second injection can be clearly seen by comparing the results for cases 2-5 with those of case 1 in which a single injection is adopted. In multiple injection cases, during the dwell time between the injections, which starts at $t = 0.6ms$, the rich zone is not fed and it gives an extra time for air entrainment to the rich zone. Hence, the pick of the mass of fuel-rich mixture in multiple injection cases is lower than that in the single injection case. The longer dwell time, the more extra time for entraining air and the lower peak of the mass in the rich zone.

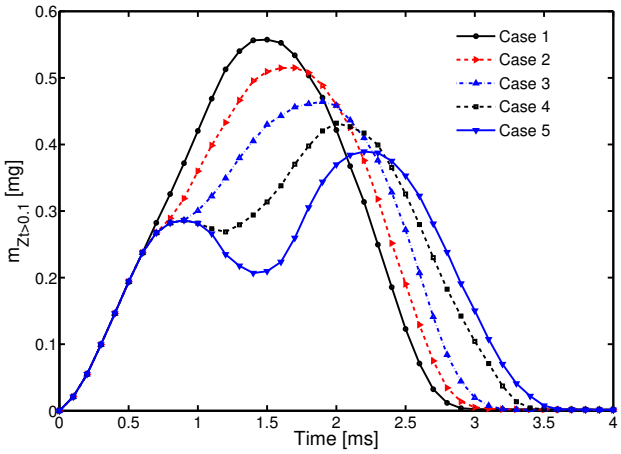

Figure 15: Total mass of the region with a mixture fraction of $Z_t \geq 0.1$.

5. Conclusion

In this work, we studied the role of injection strategies on jet-jet interaction, fuel-air mixing, penetration, and near-nozzle mixture in multiple injection strategies. To investigate the effect of dwell timing, injection splitting strategies, and mass flow rate of post-injection on these parameters, fourteen injection strategies were examined. The results showed that the second injection penetrates into the domain faster than the main injection. This is due to the history effect of the first injection in the domain. When a post-injection penetrates into the main injection, it increases the turbulence intensity of the main injection. As a result of this, the local scalar dissipation rate is increased, which in turn enhances the mixing rate.

The level of penetration of the second injection into the first injection and the interaction of two injections are sensitive to the dwell timing between the two consecutive injections. In the cases with longer dwell time this penetration is horter and jet-jet interaction is lower than that in cases with shorter dwell time. Other major factors affecting the interaction of two injections are the duration and momentum of the post-injection. Results showed that a weak and short post-injection cannot alert the flow field resulted from the main injection. In such scenarios even with short dwell timing, the mixing process of the main injection is not substantially affected by the second injection.

Although a weak and short post-injection does not contribute to the mixing of the main injection, however, it can be very important due to another mechanism. It is known that the near-nozzle region during a ramp-down period is rapidly becoming lean and the mixture equivalence ratio can potentially fall below the flammability limit. A short post-injection can either be optimized to have a high momentum and push the near-nozzle gases formed during the main injection farther downstream where there is a much better mixing and combustion condition, or have a low momentum for the fuel to remain near the nozzle and enrich the fuel-lean near-nozzle residue of the first injection. The key point to the optimization of a post-injection in this regard is to optimize the momentum of the post-injection.

Despite the interaction of two injections, the dwell time gives an extra time for the injected gas to entrain more air and this reduces the mass of the rich zone. In the strategies with longer dwell time, more time is given for the gas to entrain air. Hence, the fuel-rich region in these strategies is smaller than that in a single injection.

Acknowledgments

This work was sponsored by the Swedish Research Council (VR). The computation was performed using the computer facilities provided by the Swedish National Infrastructures for Computing (SNIC at HPC2N and PDC).

Refrences

[1] José M Desantes, Jean Arrègle, J Javier López, and Antonio García. A comprehensive study of diesel combustion and emissions with post-injection. Technical report, SAE Technical Paper, 2007.

[2] Zhiyu Han, All Uludogan, Gregory J Hampson, and Rolf D Reitz. Mechanism of soot and nox emission reduction using multiple-injection in a diesel engine. Technical report, SAE Technical Paper, 1996.
[3] Jacqueline O'Connor and Mark Musculus. Post injections for soot reduction in diesel engines: a review of current understanding. *SAE International Journal of Engines*, 6(2013-01-0917):400–421, 2013.
[4] Ahmed Abdul Moiz, Muhsin M Ameen, Seong-Young Lee, and Sibendu Som. Study of soot production for double injections of n-dodecane in ci engine-like conditions. *Combustion and Flame*, 173:123–131, 2016.
[5] Jacqueline O'Connor and Mark Musculus. Optical investigation of the reduction of unburned hydrocarbons using close-coupled post injections at ltc conditions in a heavy-duty diesel engine. *SAE International Journal of Engines*, 6(2013-01-0910):379–399, 2013.
[6] Randy Hessel, Rolf D Reitz, Mark Musculus, Jacqueline O'Connor, and Daniel Flowers. A cfd study of post injection influences on soot formation and oxidation under diesel-like operating conditions. *SAE International Journal of Engines*, 7(2014-01-1256):694–713, 2014.
[7] Hanho Yun and Rolf D Reitz. An experimental investigation on the effect of post-injection strategies on combustion and emissions in the low-temperature diesel combustion regime. *Journal of Engineering for Gas Turbines and Power*, 129(1):279–286, 2007.
[8] Rickard Ehleskog and Raúl L Ochoterena. Soot evolution in multiple injection diesel flames. Technical report, SAE Technical Paper, 2008.
[9] André Sperl. The influence of post-injection strategies on the emissions of soot and particulate matter in heavy duty euro v diesel engine. Technical report, SAE Technical Paper, 2011.
[10] Sylvain Mendez and Benoist Thirouard. Using multiple injection strategies in diesel combustion: potential to improve emissions, noise and fuel economy trade-off in low cr engines. *SAE International Journal of Fuels and Lubricants*, 1(2008-01-1329):662–674, 2008.
[11] Mohan Bobba, Mark Musculus, and Wiley Neel. Effect of post injections on in-cylinder and exhaust soot for low-temperature combustion in a heavy-duty diesel engine. *SAE International Journal of Engines*, 3(2010-01-0612):496–516, 2010.
[12] A Vanegas, H Won, C Felsch, M Gauding, and N Peters. Experimental investigation of the effect of multiple injections on pollutant formation in a common-rail di diesel engine. Technical report, SAE Technical Paper, 2008.
[13] Yoshihiro Hotta, Minaji Inayoshi, Kiyomi Nakakita, Kiyoshi Fujiwara, and Ichiro Sakata. Achieving lower exhaust emissions and better performance in an hsdi diesel engine with multiple injection. Technical report, SAE Technical Paper, 2005.
[14] DA Pierpont, DT Montgomery, and Rolf D Reitz. Reducing particulate and nox using multiple injections and egr in a di diesel. Technical report, SAE Technical Paper, 1995.
[15] Christophe Barro, Frédéric Tschanz, Peter Obrecht, and Konstantinos Boulouchos. Influence of post-injection parameters on soot formation and oxidation in a common-rail-diesel engine using multi-color-pyrometry. *ASME Paper No. ICEF2012-92075*, 2012.
[16] Santiago Molina, José Maria Desantes, Antonio Garcia, and José M Pastor. A numerical investigation on combustion characteristics with the use of post injection in di diesel engines. Technical report, SAE Technical Paper, 2010.
[17] Jean Arrègle, José V Pastor, J Javier López, and Antonio García. Insights on postinjection-associated soot emissions in direct injection diesel engines. *Combustion and Flame*, 154(3):448–461, 2008.
[18] Takaaki Kitamura, T Ito, Jiro Senda, and Hajime Fujimoto. Mechanism of smokeless diesel combustion with oxygenated fuels based on the dependence of the equivalence ration and temperature on soot particle formation. *International Journal of Engine Research*, 3(4):223–248, 2002.
[19] Bing Hu, Mark PB Musculus, and Joseph C Oefelein. The influence of large-scale structures on entrainment in a decelerating transient turbulent jet revealed by large eddy simulation. *Physics of Fluids*, 24(4):045106, 2012.
[20] Meghan J Borz, Yoontak Kim, and Jacqueline O'Connor. The effects of injection timing and duration on jet penetration and mixing in multiple-injection schedules. Technical report, SAE Technical Paper, 2016.
[21] Yuanjiang Pei, Evatt R Hawkes, and Sanghoon Kook. Transported probability density function modelling of the vapour phase of an n-heptane jet at diesel engine conditions. *Proceedings of the Combustion Institute*, 34(2):3039–3047, 2013.
[22] John Abraham and Lyle M Pickett. Computed and measured fuel vapor distribution in a diesel spray. *Atomization and sprays*, 20(3), 2010.
[23] Cheng Gong, Mehdi Jangi, and Xue-Song Bai. Large eddy simulation of n-dodecane spray combustion in a high pressure combustion vessel. *Applied Energy*, 136:373–381, 2014.
[24] Peter O Witze. Hot-film anemometer measurements in a starting turbulent jet. *AIAA Journal*, 21(2):308–309, 1983.
[25] Peter O Witze. Impulsively started incompressible turbulent jet. Technical report, Sandia Labs., Livermore, CA (USA), 1980.
[26] Stephen B Pope. Turbulent flows, cambridge university press, pp. 96-101, 2001.
[27] Hussein J Hussein, Steven P Capp, and William K George. Velocity measurements in a high-reynolds-number, momentum-conserving, axisymmetric, turbulent jet. *Journal of Fluid Mechanics*, 258:31–75, 1994.
[28] Clément Chartier, Oivind Andersson, Bengt Johansson, Mark Musculus, and Mohan Bobba. Effects of post-injection strategies on near-injector over-lean mixtures and unburned hydrocarbon emission in a heavy-duty optical diesel engine. *SAE International Journal of Engines*, 4(2011-01-1383):1978–1992, 2011.
[29] Jacqueline O'Connor, Mark PB Musculus, and Lyle M Pickett. Effect of post injections on mixture preparation and unburned hydrocarbon emissions in a heavy-duty diesel engine. *Combustion and Flame*, 170:111–123, 2016.
[30] Ahmad Hadadpour, Mehdi Jangi, and Xue Song Bai. The effect of splitting timing on mixing in a jet with double injections: A large-eddy simulation study. *Flow, Turbulence and Combustion*, pages 1–15, 2018.
[31] Heinz Pitsch and Helfried Steiner. Scalar mixing and dissipation rate in large-eddy simulations of non-premixed turbulent combustion. *Proceedings of the Combustion Institute*, 28(1):41–49, 2000.
[32] Sharath S Girimaji and Ye Zhou. Analysis and modeling of subgrid scalar mixing using numerical data. *Physics of Fluids*, 8(5):1224–1236, 1996.
[33] Khanh Cung, Abdul Moiz, Jaclyn Johnson, Seong-Young Lee, Chol-Bum Kweon, and Alessandro Montanaro. Spray–combustion interaction mechanism of multiple-injection under diesel engine conditions. *Proceedings of the Combustion Institute*, 35(3):3061–3068, 2015.